Towards 3D Mapping of BO_6 Octahedron Rotations at Perovskite Heterointerfaces, Unit Cell by Unit Cell

Qian He,*,† Ryo Ishikawa,†,∥ Andrew R. Lupini,†,‡ Liang Qiao,§ Eun J. Moon,⊥ Oleg Ovchinnikov,‡,# Steven J. May,⊥ Michael D. Biegalski,§,▽ and Albina Y. Borisevich*,†,‡,§

†Materials Science and Technology Division, ‡Institute for Functional Imaging of Materials, and §The Center for Nanophase Materials Sciences, Oak Ridge National Laboratory, Oak Ridge, Tennessee 37831, United States, ∥Institute of Engineering Innovation, The University of Tokyo, 2-11-16, Yayoi, Bunkyo-ku, Tokyo 113-8656, Japan, ⊥Department of Materials Science and Engineering, Drexel University, Philadelphia, Pennsylvania 19104, United States, and #Department of Physics and Astronomy, Vanderbilt University, Nashville, Tennessee 37240, United States

ABSTRACT The rich functionalities in the ABO_3 perovskite oxides originate, at least in part, from the ability of the corner-connected BO_6 octahedral network to host a large variety of cations through distortions and rotations. Characterizing these rotations, which have significant impact on both fundamental aspects of materials behavior and possible applications, remains a major challenge at heterointerfaces. In this work, we have developed a unique method to investigate BO_6 rotation patterns in complex oxides ABO_3 with unit cell resolution at heterointerfaces, where novel properties often emerge. Our method involves column shape analysis in ABF-STEM images of the ABO_3 heterointerfaces taken in specific orientations. The rotating phase of BO_6 octahedra can be identified for all three spatial dimensions without the need of case-by-case simulation. In several common rotation systems, quantitative measurements of all three rotation angles are now possible. Using this method, we examined interfaces between perovskites with distinct tilt systems as well as interfaces between tilted and untilted perovskites, identifying an unusual coupling behavior at the $CaTiO_3$/LSAT interface. We believe this method will significantly improve our knowledge of complex oxide heterointerfaces.

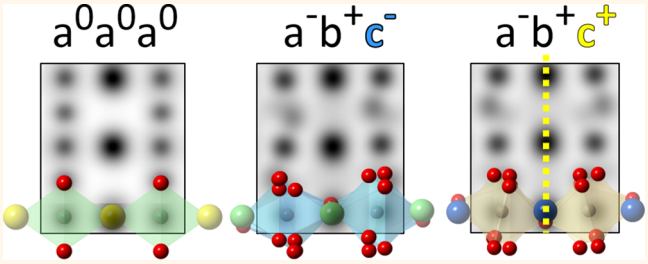

KEYWORDS: octahedral rotations · complex oxides · scanning transmission electron microscopy · interfaces

The family of ABO_3 perovskite oxides is a veritable gold mine of diverse physical properties, due largely to the ability of the structure to host a wide variety of metal cations on both A and B sites. When the size of the A cation is smaller than required for the perfect cubic unit cell, it is accommodated *via* the rotations of the BO_6 octahedral network (also known as octahedral tilt).[1−4] These changes can in turn alter the B−O bond lengths, the B−O−B bond angles and therefore the electronic and magnetic behavior of the material, resulting in complex coupled phenomena. Additional complexity arises at epitaxial heterointerfaces due to built-in discontinuities of one or more of the charge, orbital, spin, lattice and stoichiometry degrees of freedom.[5−10] While the possibilities of engineering desired interfacial properties through epitaxial strain and substrate composition are widely explored, it has only recently been recognized that interfacial coupling of the BO_6 octahedral networks with different symmetries can also be a powerful route.[11,12] Surprising material functionalities have already been shown to emerge *via* engineering BO_6 rotations: for example, theoretical approaches have been applied to predict nonconventional ferroelectricity induced by BO_6 rotations, while in bulk material such rotations usually result in suppression of ferroelectric behavior.[13−16] Examples of experimental studies include BO_6 rotation controlled polar order in $BiFeO_3$,[17] increased Curie temperature in $La_{0.7}Sr_{0.3}MnO_3$ (LSMO)/$Eu_{0.7}Sr_{0.3}MnO_3$ (ESMO) superlattices,[18] altered magnetization and electrical conductivity in LSMO thin films,[19] and modified magnetic properties in $La_{0.5}Sr_{0.5}CoO_3$.[20] Notably, BO_6 rotation engineering has recently been applied to generate room temperature electric polar and weak ferromagnetic behavior in the layered perovskite $(Ca_ySr_{1-y})_{1.15}Tb_{1.85}Fe_2O_7$,

* Address correspondence to heqian.lehigh@gmail.com, albinab@ornl.gov.

Received for review May 28, 2015 and accepted July 15, 2015.

Published online July 15, 2015
10.1021/acsnano.5b03232

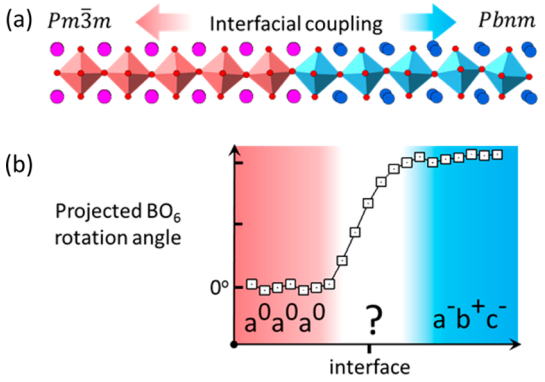

Figure 1. Schematic of an atomically abrupt but structurally diffuse heterointerface for expitaxially grown ABO_3 perovskite materials. (a) The polyhedral model shows an interface between two ABO_3 with different symmetries (in this case $Pm\bar{3}m$ and $Pbnm$), with an interfacial coupling region around the interface. (b) Existing methods allow BO_6 rotation to be measured as projected angles on the image plane, and to be plotted as a profile across the interface (tick marks reflect arbitrary scale). However, new methods are needed to determine the full 3D symmetry of the BO_6 rotations (shown as overlaid colors: red, $a^0a^0a^0$; blue, $a^-b^+c^-$; white, unknown).

further demonstrating the significance of this strategy.[21]

To fully understand the heterostructures created using this new route, we need to identify the BO_6 rotations, ideally both the symmetry and the magnitude, as a function of the distance from the heterointerface. This is a major challenge. Figure 1 shows a hypothetical heterostructure between two ABO_3 perovskites with different bulk symmetries (in this case $Pm\bar{3}m$ and $Pbnm$). Their BO_6 rotation patterns can be conventionally described by using Glazer's notation[3] as $a^0a^0a^0$ and $a^-b^+c^-$, respectively. The letters represent, respectively, the rotation angles α, β, and γ along pseudocubic $[100]_{pc}$, $[010]_{pc}$, and $[001]_{pc}$ axes (in this work, we define the out-of-plane direction as $[001]_{pc}$, which is the film growth direction). If the same letter is used for different axes, the corresponding rotation angles have same magnitude. The superscripts describe the symmetry of rotation between adjacent BO_6 units along the respective axes: "+" stands for in-phase rotations, meaning that they are rotating in the same direction, and thus a mirror plane normal to the rotation axis exists; "−" stands for out-of-phase rotations, meaning that they are rotating in opposite directions; "0" means no rotation. As shown in Figure 1a, the transition from one symmetry to another creates an interfacial coupling region where symmetry cannot be *a priori* known and the BO_6 units themselves undergo additional distortions in order to maintain their corner connectivity. The length scale of the symmetry interfacial coupling was previously reported to be two to eight unit cells wide, significantly smaller than the effective range of epitaxial strain.[22−28] Existing techniques that probe BO_6 rotations from reciprocal space (e.g., synchrotron X-ray[29] and electron diffractions[30,31]) do not yet have high enough spatial resolution for heterointerfaces. Aberration corrected electron microscopy imaging techniques, such as negative Cs high resolution TEM,[22] bright field (BF)[23] and annular bright field (ABF)[27,32] STEM were used to map BO_6 projected rotations by directly imaging oxygen atoms in real space, and the interfacial coupling region can be presented in the profile of projected rotation angle across the heterointerface (Figure 1b). However, since the BO_6 rotation is in three dimensions (3D), merely knowing one projected rotation angle is not enough to determine the full rotation pattern; in particular, this approach discounts the possibility of a distinct symmetry emerging in the out-of-plane direction in the film. Notably, recently developed techniques, such as coherent Bragg rod analysis (COBRA)[28] and position averaged convergent beam electron diffraction (PACBED),[25,33] can in principle obtain 3D information about BO_6 rotations with unit cell spatial resolution. However, each has intrinsic drawbacks: In order for COBRA to work, the film in the in-plane direction needs to be essentially defect free, as only the folded electron density is obtained,[34] while tilted perovskites are prone to mosaicism; PACBED, in turn, still relies on symmetry information in the reciprocal space, and requires intensive model based simulation.[35] Therefore, PACBED becomes very difficult for complex materials with several competing phenomena, since each sample parameter, such as thickness, polarization, strain, and tilt, adds an extra dimension to the simulation phase space. Therefore, a method that can reliably obtain 3D BO_6 rotation information at the heterointerface with unit cell resolution is still lacking.

In this work, we introduce a new method using oxygen column shape analysis in ABF-STEM. In a typical cross section specimen, rotation phases ("+", "−", or "0") for all three components of the BO_6 rotations can be quickly identified, and for some common rotation patterns quantitative information about all three rotation angles can also be obtained. We applied these methods to study two model systems, namely, a $(LSMO)_6/(ESMO)_6$ superlattice grown on $SrTiO_3$ (STO) substrate (representative of the interfaces between two different tilted symmetries) and $CaTiO_3$ (CTO) grown on $(LaAlO_3)_{0.3}(Sr_2AlTaO_6)_{0.7}$ (LSAT) substrate (representative of the interfaces of the tilted and untilted (cubic) perovskites).

RESULTS AND DISCUSSION

The reported instances of characterization of the BO_6 rotations at heterointerfaces from electron microscopy images rely solely on the position information on oxygen column projections.[22,23,27,32] However, the column position alone cannot fully describe the alignments of oxygen atoms due to the different BO_6 rotations within the column. In contrast, we have realized that the resulting distorted shape of the oxygen column projections can provide additional information.[36]

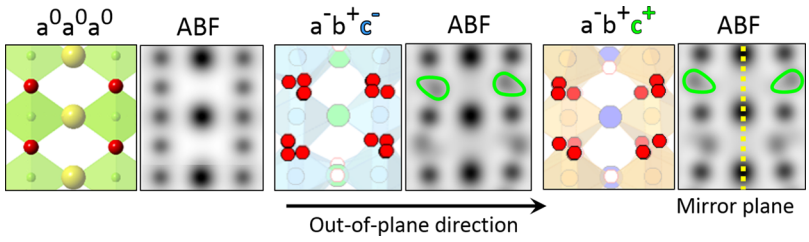

Figure 2. Qualitative 3D determination of BO_6 rotation. Atomic models and corresponding ABF images (multislice simulation using Kirkland's code[37]) of model ABO_3 perovskite structures (modeled using POTATO[38]) with (a) $a^0a^0a^0$, (b) $a^-b^+c^-$, and (c) $a^-b^+c^+$ BO_6 rotation patterns, viewed from a $[110]_{pc}$ direction. The $[001]_{pc}$ is set to be the out-of-plane direction, shown as the black arrow. The alignment of oxygen atoms in this projection depends on the BO_6 rotation pattern of the structure. Oxygen columns in the corresponding simulated ABF images are therefore no longer round but have a teardrop-like shape (outlined in green in (b) and (c)), providing 3D information about the BO_6 rotation. For example, the presence of a "+" rotation in the out-of-plane direction can be seen as a mirror plane (yellow dashed line in (c)) emerging between two adjacent oxygen columns.

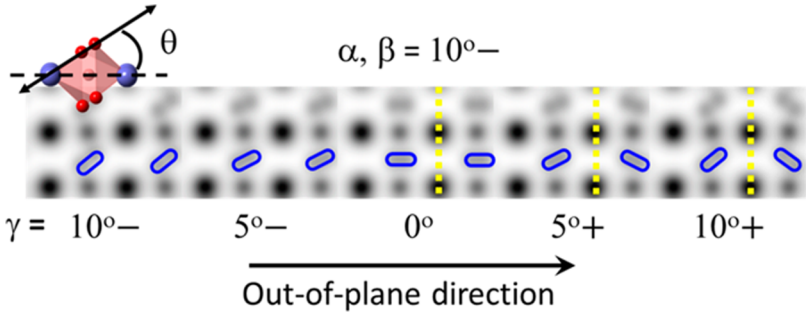

Figure 3. Quantitative 3D determination on BO_6 rotation. Simulated ABF image chart of model perovskite structures with BO_6 rotations of constant α and β but different γ. The $[001]_{pc}$ is set to be the out-of-plane direction. The overlapped polyhedral model highlights the position of oxygen columns (red) in the simulated images. The resultant oxygen column image can be considered as an ellipse (outlined in blue), due to α and β rotations both being "−". We can define an inclination angle θ between the major axis of the ellipse with respect to a reference (e.g., A−A or B−B). In this case, the magnitude of θ has a correlation with the magnitude of the γ rotation, and therefore quantitative information can be obtained by measuring θ. Yellow dashed lines indicate the mirror planes along the out-of-plane direction when γ rotation is either "+" or "0". A more detailed summary of shape analysis can be found in the Supporting Information.

Figure 2 shows three model perovskite structures with BO_6 rotations patterns of (a) $a^0a^0a^0$, (b) $a^-b^+c^-$, and (c) $a^-b^+c^+$ and their corresponding simulated ABF images,[37] viewed from the pseudocubic $[110]_{pc}$ direction. The pure oxygen columns are highlighted in red. Compared to $a^0a^0a^0$ (Figure 2a), the oxygen atoms are not aligned but split into multiple columns in the cases of $a^-b^+c^-$ (Figure 2b) and $a^-b^+c^+$ (Figure 2c), Although the projected separation of the oxygen atoms is usually so small (e.g., <0.3 Å) that it cannot yet be resolved even with a state-of-the-art STEM, changes can be observed. The image of the oxygen columns will no longer appear not circular, but teardrop-like in shape (outlined in green), preserving the key symmetry information. For instance, the adjacent oxygen columns in the structure with "+" rotation seem to be related *via* a mirror plane (denoted by a yellow dashed line in Figure 2c), while for "−" rotation (Figure 2b) there is no such mirroring. This allows the qualitative information about BO_6 rotation in the out-of-plane direction to be obtained from a cross-section view of the heterointerface. Previously extracting this information at the heterointerface would have require a plan view specimen with the substrate removed, resulting in inevitable changes of the original epitaxial state, and also making impossible studies of the structure as a function of distance from the interface.

Furthermore, in some cases, a quantitative determination of the BO_6 rotation in 3D can be obtained. Figure 3 shows a sequence of simulated ABF images of model perovskite structures where α and β are both held constant at (10°, "−") and γ ranges from (10°, "−") to (10°, "+"). Compared with Figure 2, the oxygen columns shown in Figure 3 have elliptical shape (outlined in blue). We can denote the inclination angle of the major axis of these ellipses as θ; this angle is clearly correlated with the magnitude of γ rotation and can therefore be used to quantify γ.

A related practical example can be found in $(LSMO)_6/(ESMO)_6$ superlattice grown on STO. In the bulk form, LSMO has a rhombohedral structure with $a^-a^-a^-$ tilt pattern, while ESMO has an orthorhombic lattice with $a^-a^-c^+$ tilt pattern. Representative STEM HAADF and ABF images of the LSMO/ESMO interfaces are shown in Figure 4a. The oxygen columns in both LSMO and ESMO regions all appear to be elliptical in shape, similar to the model case in Figure 3. A change in γ rotation phase can be visually detected as a mirror

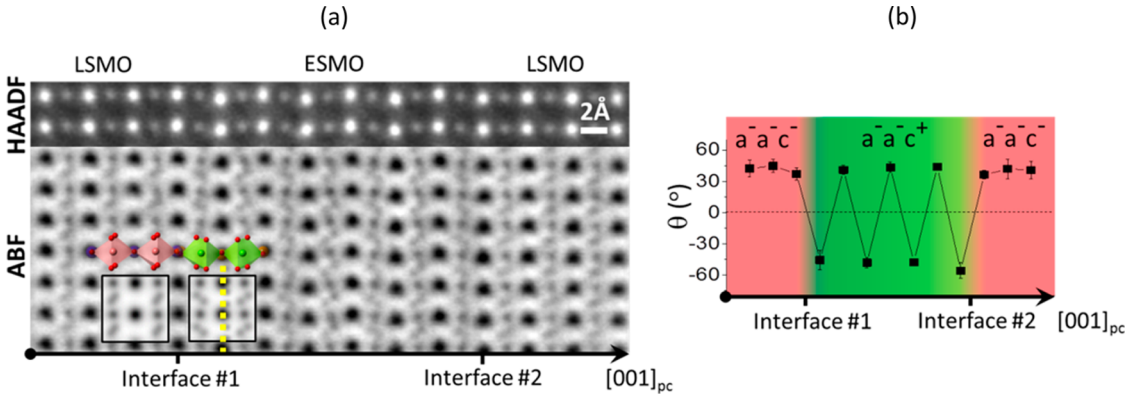

Figure 4. Interfaces in the (LSMO)6/(ESMO)6 superlattice on STO substrate. (a) Experimental STEM HAADF and ABF images of the LSMO/ESMO interfaces along one $[110]_{pc}$ axis, with overlapped polyhedral model and the simulated ABF images (insets). The $[001]_{pc}$ direction for both oxides is the out-of-plane direction, which is the film growth direction. (b) Plane averaged profile of θ, measured from the image in (a) with respect to the direction defined by adjacent B sites. The symmetries of BO_6 rotation across the interfaces are displayed as the overlaid colors (red, $a^-a^-c^-$; green, $a^-a^-c^+$), which are determined from θ angle measurement and other analysis, such as PCA (see text and Supporting Information for more details).

plane (shown as a yellow dashed line) that arises between adjacent oxygen columns along the out-of-plane direction. Figure 4b shows the plane averaged inclination angle θ of the major axes of the oxygen column ellipses as a function of coordinate along the out-of-plane direction. The emergence of "+" γ rotation in the ESMO layer can be seen as θ with alternating signs. The magnitude of θ appears constant within both LSMO and ESMO layers, with no interfacial effects, indicating that the γ rotation phase changes abruptly. This is possible as the phase of the γ rotation does not alter the position of the apical oxygen atom that bridges the two materials.

Spatial correlations and local symmetries such as those found in tilted perovskite images are also well suited for automatic identification with multivariate methods.[36] In Figure S1, we show how local symmetry relations in ESMO/LSMO superlattices can be revealed by principal component analysis (PCA) of the oxygen column shapes. Similarly to the quantification approach described above, PCA results show that the rotation transition in this particular superlattice is abrupt.

When faced with a broader task of identifying unknown tilt symmetry from a STEM image, one needs to have a more complete understanding of the correspondence of the oxygen column shapes and their symmetry relations to the 3D BO_6 rotation systems. Figure 3 provides a one-dimensional glimpse of such a pattern; the full phase space in this case is three-dimensional (α, β, and γ), with some simplifications due to interchangeability of α and β. To build this comprehensive view and outline additional routes for characterization of three-dimensional tilted structures, we simulated the images for all the possible tilted perovskite symmetries for 5° steps in tilt angles using atomic models generated by POTATO.[38] Figure S2 shows several nonredundant excerpts from the tilt phase space: the origin, i.e. the simulated image of the untilted perovskite (Figure S2a), and two 2D slices we term ABF navigation charts, for different BO_6 rotation patterns: constant β rotation (10°, "−") with varying α and γ (Figure S2b) and constant γ rotation (10°, "−") with varying α and β (Figure S2c). All the images in these charts are simulated in $[110]_{pc}$ orientation; for structures such as rhombohedral perovskites with two inequivalent $[110]_{pc}$ directions, $[0\bar{1}1]_R$ projection was used (see Figure S3).

Examination of these charts allows us to formulate general rules for characterization of 3D BO_6 rotation information; the rules are summarized in Table S1. For instance, we found that (i) the symmetry of individual columns and (ii) the symmetry between columns can be used to quickly identify rotation phases in all three $[001]_{pc}$ directions. Furthermore, (iii) the apparent tilt angle of the oxygen column centroids and (iv) the inclination angle of oxygen columns can provide quantitative information about rotation angles in many cases. Notice that there is usually no one to one correlation in Table S1, meaning that multiple features need to be considered simultaneously to draw a conclusion. We have also analyzed the effect of the possible imaging artifacts, including residual probe coma aberrations up to 200 nm (Figure S4), and sample mistilt up to 5 mrad (Figure S5), and concluded that these artifacts do not generate features that can be confused with those discussed above.

This broader understanding given by Figure S2 and Table S1 was indispensable for interpreting our observations of the CTO/LSAT interface. In bulk, CTO has an orthorhombic structure with $a^-a^-c^+$ pattern, while LSAT has a cubic lattice with $a^0a^0a^0$ pattern. Figure S6(a) shows the STEM images of the CTO/LSAT interface along $[010]_{pc}$ direction, in which an in-phase rotation of BO_6 octahedra can be directly detected. The HAADF image shows the interface to be atomically sharp, as the CTO film appears much darker compared

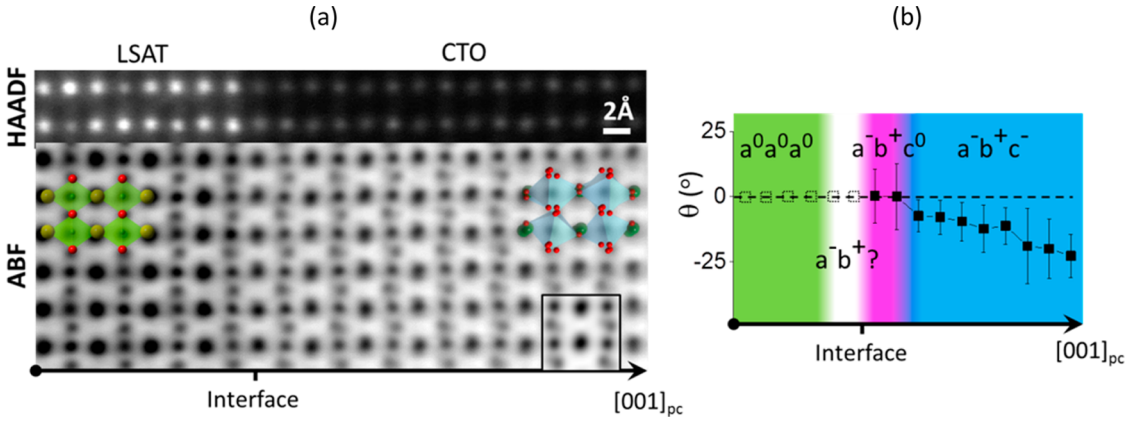

Figure 5. Interface of the CTO film and the LSAT substrate with a transition layer of a different BO_6 rotation pattern. (a) STEM HAADF and ABF images of the CTO/LSAT interface along $[110]_{pc}$ axis, with overlapped polyhedral model and one simulated ABF image (inset). The $[001]_{pc}$ direction for both oxides is the out-of-plane direction, which is the film growth direction. (b) Plane averaged profile of θ. The solid squares are measured values, and the empty squares are speculated values for the LSAT substrate, where there is no well-defined deviation from roundness to detect. Symmetries of BO_6 rotation across the interfaces are displayed as overlaid colors (green, $a^0a^0a^0$; white, a^-b^+?; purple, $a^-b^+c^0$; blue $-$ $a^-b^+c^-$), which are determined from θ angle measurement as well as other analysis, such as PCA (see text and Supporting Information). In contrast to the case of the LSMO/ESMO interface (see Figure 4), a distinct BO_6 rotation pattern (purple, $a^-b^+c^0$) is found in the transitional layer at the interface.

to the LSAT substrate, consistent with much lower atomic numbers of the constituent elements. The interfacial coupling region was found to extend to five to six unit cells from the interface; within this region, the β rotation angle gradually changes from around 10° in the CTO film to 0° in the LSAT substrate. β rotation with "+" phase is clearly developed in top two layers of LSAT. Such in-plane BO_6 rotation coupling is mainly due to connectivity constrains of adjacent BO_6 units and is in agreement with previous studies.[22,23,27,32]

We can further obtain 3D information about BO_6 rotations at this interface. Figure 5a shows the STEM images of CTO/LSAT interface looking down the $[110]_{pc}$. The oxygen columns in CTO region appear to be teardrop-like in shape. We can therefore confirm that the in-plane rotation components α and β are "+" and "−", respectively, which agrees with the results in Figure S6. The PCA analysis of the oxygen column shapes (Figure S7a−c) shows that the first component has one bright spot at lower right corner and a dark spot at the opposite, consistent with the rotated teardrop shape. The corresponding map and the plane averaged profiles reveal a checkerboard spatial distribution of the shapes. This indicates that no mirror symmetry is present in the out-of-plane direction and thus "−" is assigned to the γ rotation for the CTO film starting from the first layer at the interface. The average PCA weight factors for the LSAT layers are close to zero, showing that the oxygen column shapes in that area of the image are close to round, probably due to a small rotation angle in the in-plane direction (Figure S6). Therefore, the presence and phase of the γ rotations cannot be determined from the column shapes alone. Nevertheless, we found that at least the top two layers of LSAT have nonzero apparent tilting of the oxygen column centroids (Figure S7d−f), suggesting that the in-plane components of the BO_6 rotations are either "+" and "−", or two "−" but not equal in magnitude or "+" and "0" (Table S1). Since we observed a "+" rotation from the $[010]_{pc}$ specimen from the top two layers of LSAT substrate, we can infer that "+" and "−" rotations are developed in plane, following the symmetry of the film in both directions.

Interestingly, when measuring the inclination angle of the oxygen columns, we clearly observed that the averaged value of θ in the first two layers of CTO was zero, which is significantly different than that of the CTO film away from the heterointerface, despite the relatively large error bars due to weak signal-to-noise ratios in the oxygen images. Because in-plane rotations in the CTO film are already confirmed to be "+" and "−.", we can rule out other possibilities described in Table S1 and directly correlate the zero θ to a zero out-of-plane γ rotation. Therefore, a distinct BO_6 rotation pattern, namely, $a^-b^+c^0$, was found in the first two layers of CTO at this heterointerface. For the LSAT side of the heterointerface region, we could not do the same measurement as the aspect ratio of the ellipse is too close to 1 so that the primary axis and inclination angle are not well-defined.

The presence of a transition layer with respect to the γ rotation is rather surprising, as no direct connectivity constrain applies to this rotation; in fact the geometric constraints are similar to the LSMO/ESMO case described above where an abrupt transition was found. The tensile strain, which is sometimes known to produce this effect,[24] is also not the likely reason, since the strain coupling region is much larger than the transition region we detect. It is however reasonable to

suspect this phenomenon is due to a combined effect of connectivity constraints on α rotation and β rotation, rigidity of the BO_6 octahedral[39] and tensile strain. Further studies are required to understand this behavior.

From the above two examples, we have demonstrated that using shape analysis methods we can deduce the 3D rotation pattern of the BO_6 rotation with unit cell resolution. Different interfacial coupling behavior in perovskite heterostructures was found between different materials: abrupt changes between ESMO and LSMO, where the noninterconnected out-of-plane γ rotation was the main difference between the two sides of the heterointerface; and a distinct BO_6 rotation pattern developing in the transition region at the interface for CTO and LSAT, where the symmetry mismatch is more profound.

This method is applicable to real-world thin films containing domains and defects, which are often seen when the film is much less symmetric than the substrate. The domain structure can be observed by electron microscopy. In the areas with no overlapping domains, the BO_6 rotation coupling can be studied in all three directions using the method described in this work. Such information cannot be obtained from other techniques such as X-ray diffraction, which averages signals from a much larger volume. To obtain qualitative phase, and in some cases quantitative information, no material-specific simulation is required. This method has several limitations. For instance, if the domain sizes are too small (e.g., $\ll$10 nm), it is going to be difficult to apply this method due to extensive domain overlapping. In addition, multiple specimens with different orientations are sometimes necessary, such as in the case of two inequivalent $[110]_{pc}$ directions (Figure S3). Out-of-plane γ rotation information can be difficult to elucidate when the in-plane rotation angles are small or they have particular combinations such as two "+" (Figure S2c). Full quantitative analysis[40−44] will still require a quantitative comparison between the simulation and the experiment, which can be very difficult for practical specimens due to the nonlinear imaging nature of ABF.[45] Ultrathin specimens (several nanometers) and annular bright field phase imaging[46] can potentially relieve this problem by providing quantitative interpretable oxygen images. Future microscopy development[47] will also bring atomic resolution in specimen thickness direction (parallel to the electron beam), which might enable depth-resolved mapping of the heterointerface structure through the sample including 3D BO_6 rotation information.

CONCLUSIONS

In summary, we have developed a method to elucidate 3D BO_6 rotation information unit cell by unit cell at ABO_3 heterointerfaces from ABF-STEM images, a heretofore intractable problem. Using the developed method, we examined two heterointerfaces that displayed very different behaviors: the ESMO/LSMO interface exhibits an abrupt change between two symmetries, while an extensive interfacial layer with a distinct BO_6 rotation pattern was found at the CTO/LSAT interface. We show that abrupt changes in the out-of-plane BO_6 rotation can occur at heterointerfaces due to the invariance of the apical oxygen position to the γ rotation. We believe this new method will greatly enhance our capability to characterize the heterointerface structure, which can be used to test the existing theories and also to help design new materials with tailored interface properties.

EXPERIMENTAL SECTION

LSMO/ESMO Synthesis. The $[(La_{0.7}Sr_{0.3}MnO_3)_6/(Eu_{0.7}Sr_{0.3}MnO_3)_6]\times 8$ superlattice was grown on a $SrTiO_3$ (001) substrate in an interrupted epitaxial growth mode by oxide molecular beam epitaxy. The thickness of each $La_{0.7}Sr_{0.3}MnO_3$ (LSMO) and $Eu_{0.7}Sr_{0.3}MnO_3$ (ESMO) layer is 6 unit cells (uc), and the LSMO/ESMO bilayer is repeated 8 times (total thickness of the superlattice is 96 uc). During deposition, the temperature of the substrate was kept at ~600 °C and an ozone/oxygen mixture (approximately 5/95%) was used as the oxidizing agent at a chamber pressure of $\sim 8.5 \times 10^{-6}$ Torr.[19,48]

CTO/LSAT Synthesis. $CaTiO_3$ films were grown by pulsed laser deposition (PLD) on LSAT using a polycrystalline $CaTiO_3$ ceramic target synthesized by solid state method. The films were grown in 100 mTorr pressure at substrate temperature of 650 °C with a laser fluence of 1.5 J/cm^2. LSAT substrates were air-annealed at 1000 C for 2 h to improve the crystalline and surface quality for epitaxial growth. The CTO films have roughness on the order of 1 unit cell and grew in a layer-by-layer growth mode as evidenced from reflection high energy electron diffraction oscillations. The film thickness was limited to ~10 nm to prevent relaxation of the epitaxial strain which was found to occur for thicknesses exceeding ~20 nm. X-ray diffraction indicated that both films were fully commensurate with the substrate with cube-on-cube-type epitaxy.

Scanning Transmission Electron Microscopy (STEM). Cross-sectional specimen oriented along $[110]_{pc}$ direction for STEM analysis were prepared by conventional mechanical thinning, precision polishing and ion milling. HAADF and ABF STEM images were taken using Nion UltraSTEM operating at 200 kV, equipped with a cold field-emission electron gun and a corrector of third- and fifth-order aberrations. The convergence semiangle for the electron probe was about 30 mrad. HAADF signals for the samples were collected from a detector angle range with an inner collection angle of ~63 mrad. Thirty quickly scanned images (0.5 μs/pixel, with pixel size of 5−10 pm), were aligned *via* autocorrelation and displayed as sum image, which has been wiener filtered to reduce noise. Image analysis was done *via* Digital micrograph and ImageJ scripts.

STEM Image simulation. The image simulations were carried out with a 200 kV probe with a probe-forming aperture half angle of 30 mrad and an ABF detector spanning the range 15−30 mrad, using the Kirkland's multislice code. 20 frozen phonon configuration was computed. The probe size was set to be 0.7 Angstrom, following reference 44.

Conflict of Interest: The authors declare no competing financial interest. ▽M.D.B.: Deceased.

Supporting Information Available: Additional figures discussed in the text. The Supporting Information is available free

of charge on the ACS Publications website at DOI: 10.1021/acsnano.5b03232.

Acknowledgment. Electron microscopy research (Q.H., R.I., A.R.L., and A.Y.B.) is supported by the U.S. Department of Energy, Office of Science, Basic Energy Sciences, Materials Sciences and Engineering Division. R.I. acknowledges support from JSPS Postdoctoral Fellowship for Research Abroad. Q.H. partly used resources of NERSC supported by the Office of Science of the U. S. DOE under Contract No. DE-AC02-05CH11231. Data analysis supported in part (O.O.) by ORNL's Laboratory Directed Research and Development (LDRD) fund. CTO/LAST is supplied by L.Q. and M.B., supported by ORNL's Center for Nanophase Materials Sciences, sponsored by the Scientific User Facilities Division, Office of Science, Basic Energy Sciences, U.S. Department of Energy. ESMO/LSMO/STO is prepared in Drexel University (E.M. and S.M.), supported by the US Army Research Office under grant No. W911NF-12-1-0132. Q.H. would like to thank Professor P. Woodward at Ohio State University for his advice regarding perovskite model generation using POTATO. Finally, this paper is dedicated to the memory of one of the authors, Dr. Michael D. Biegalski, who recently passed away.

REFERENCES AND NOTES

1. Woodward, P. M. Octahedral Tilting in Perovskites. I. Geometrical Considerations. *Acta Crystallogr., Sect. B: Struct. Sci.* **1997**, *53*, 32–43.
2. Woodward, P. M. Octahedral Tilting in Perovskites. II. Structure Stabilizing Forces. *Acta Crystallogr., Sect. B: Struct. Sci.* **1997**, *53*, 44–66.
3. Glazer, A. The Classification of Tilted Octahedra in Perovskites. *Acta Crystallogr., Sect. B: Struct. Crystallogr. Cryst. Chem.* **1972**, *28*, 3384–3392.
4. Glazer, A. A Brief History of Tilts. *Phase Transitions* **2011**, *84*, 405–420.
5. Kalinin, S. V.; Borisevich, A.; Fong, D. Beyond Condensed Matter Physics on the Nanoscale: The Role of Ionic and Electrochemical Phenomena in the Physical Functionalities of Oxide Materials. *ACS Nano* **2012**, *6*, 10423–10437.
6. Hwang, H. Y.; Iwasa, Y.; Kawasaki, M.; Keimer, B.; Nagaosa, N.; Tokura, Y. Emergent Phenomena at Oxide Interfaces. *Nat. Mater.* **2012**, *11*, 103–113.
7. Bhattacharya, A.; May, S. J. Magnetic Oxide Heterostructures. *Annu. Rev. Mater. Res.* **2014**, *44*, 65–90.
8. Mannhart, J.; Schlom, D. G. Oxide Interfaces--an Opportunity for Electronics. *Science* **2010**, *327*, 1607–1611.
9. Demkov, A. A.; Posadas, A.; Seo, H.; Lee, J. K.; Sai, N. Emerging Physics of Oxide Heterostructures. *Phys. Status Solidi B* **2011**, *248*, 2076–2081.
10. Zubko, P.; Gariglio, S.; Gabay, M.; Ghosez, P.; Triscone, J.-M. Interface Physics in Complex Oxide Heterostructures. *Annu. Rev. Condens. Matter Phys.* **2011**, *2*, 141–165.
11. Rondinelli, J. M.; Spaldin, N. A. Substrate Coherency Driven Octahedral Rotations in Perovskite Oxide Films. *Phys. Rev. B: Condens. Matter Mater. Phys.* **2010**, *82*, 113402.
12. Rondinelli, J. M.; May, S. J.; Freeland, J. W. Control of Octahedral Connectivity in Perovskite Oxide Heterostructures: An Emerging Route to Multifunctional Materials Discovery. *MRS Bull.* **2012**, *37*, 261–270.
13. Benedek, N. A.; Mulder, A. T.; Fennie, C. J. Polar Octahedral Rotations: A Path to New Multifunctional Materials. *J. Solid State Chem.* **2012**, *195*, 11–20.
14. Rondinelli, J. M.; Fennie, C. J. Octahedral Rotation-Induced Ferroelectricity in Cation Ordered Perovskites. *Adv. Mater.* **2012**, *24*, 1961–1968.
15. Benedek, N. A.; Fennie, C. J. Hybrid Improper Ferroelectricity: A Mechanism for Controllable Polarization-Magnetization Coupling. *Phys. Rev. Lett.* **2011**, *106*, 107204.
16. Bousquet, E.; Dawber, M.; Stucki, N.; Lichtensteiger, C.; Hermet, P.; Gariglio, S.; Triscone, J.-M.; Ghosez, P. Improper Ferroelectricity in Perovskite Oxide Artificial Superlattices. *Nature* **2008**, *452*, 732–736.
17. Kim, Y.-M.; Kumar, A.; Hatt, A.; Morozovska, A. N.; Tselev, A.; Biegalski, M. D.; Ivanov, I.; Eliseev, E. A; Pennycook, S. J.; Rondinelli, J. M.; et al. Interplay of Octahedral Tilts and Polar Order in BiFeO3 Films. *Adv. Mater.* **2013**, *25*, 2497–2504.
18. Moon, E. J.; Colby, R.; Wang, Q.; Karapetrova, E.; Schlepütz, C. M.; Fitzsimmons, M. R.; May, S. J. Spatial Control of Functional Properties *via* Octahedral Modulations in Complex Oxide Superlattices. *Nat. Commun.* **2014**, *5*, 5710.
19. Moon, E. J.; Balachandran, P. V.; Kirby, B. J.; Keavney, D. J.; Sichel-Tissot, R. J.; Schlepütz, C. M.; Karapetrova, E.; Cheng, X. M.; Rondinelli, J. M.; May, S. J. Effect of Interfacial Octahedral Behavior in Ultrathin Manganite Films. *Nano Lett.* **2014**, *14*, 2509–2514.
20. Biegalski, M. D.; Takamura, Y.; Mehta, A.; Gai, Z.; Kalinin, S. V.; Ambaye, H.; Lauter, V.; Fong, D.; Pantelides, S. T.; Kim, Y. M.; et al. Interrelation between Structure - Magnetic Properties in La 0.5 Sr 0.5 CoO 3. *Adv. Mater. Interfaces* **2014**, *1*, 1400203.
21. Pitcher, M. J.; Mandal, P.; Dyer, M. S.; Alaria, J.; Borisov, P.; Niu, H.; Claridge, J. B.; Rosseinsky, M. J. Tilt Engineering of Spontaneous Polarization and Magnetization above 300 K in a Bulk Layered Perovskite. *Science (Washington, DC, U. S.)* **2015**, *347*, 420–424.
22. Jia, C.; Mi, S.; Faley, M.; Poppe, U.; Schubert, J.; Urban, K. Oxygen Octahedron Reconstruction in the SrTiO3/LaAlO3 Heterointerfaces Investigated Using Aberration-Corrected Ultrahigh-Resolution Transmission Electron Microscopy. *Phys. Rev. B: Condens. Matter Mater. Phys.* **2009**, *79*, 081405.
23. Borisevich, A. Y.; Chang, H. J.; Huijben, M.; Oxley, M. P.; Okamoto, S.; Niranjan, M. K.; Burton, J. D.; Tsymbal, E. Y.; Chu, Y. H.; Yu, P.; et al. Suppression of Octahedral Tilts and Associated Changes in Electronic Properties at Epitaxial Oxide Heterostructure Interfaces. *Phys. Rev. Lett.* **2010**, *105*, 087204.
24. May, S. J.; Smith, C. R.; Kim, J.-W.; Karapetrova, E.; Bhattacharya, A.; Ryan, P. J. Control of Octahedral Rotations in $(LaNiO_3)_n/(SrMnO_3)_m$ Superlattices. *Phys. Rev. B: Condens. Matter Mater. Phys.* **2011**, *83*, 153411.
25. Zhang, J. Y.; Hwang, J.; Raghavan, S.; Stemmer, S. Symmetry Lowering in Extreme-Electron-Density Perovskite Quantum Wells. *Phys. Rev. Lett.* **2013**, *110*, 256401.
26. Aso, R.; Kan, D.; Shimakawa, Y.; Kurata, H. Octahedral Tilt Propagation Controlled by A-Site Cation Size at Perovskite Oxide Heterointerfaces. *Cryst. Growth Des.* **2014**, *14*, 2128–2132.
27. Aso, R.; Kan, D.; Shimakawa, Y.; Kurata, H. Atomic Level Observation of Octahedral Distortions at the Perovskite Oxide Heterointerface. *Sci. Rep.* **2013**, *3*, 2214.
28. Fister, T. T.; Zhou, H.; Luo, Z.; Seo, S. S. A.; Hruszkewycz, S. O.; Proffit, D. L.; Eastman, J. A.; Fuoss, P. H.; Baldo, P. M.; Lee, H. N.; et al. Octahedral Rotations in Strained LaAlO3/SrTiO3 (001) Heterostructures. *APL Mater.* **2014**, *2*, 021102.
29. May, S. J.; Kim, J.-W.; Rondinelli, J. M.; Karapetrova, E.; Spaldin, N. A.; Bhattacharya, A.; Ryan, P. J. Quantifying Octahedral Rotations in Strained Perovskite Oxide Films. *Phys. Rev. B: Condens. Matter Mater. Phys.* **2010**, *82*, 014110.
30. Woodward, D. I.; Reaney, I. M. Electron Diffraction of Tilted Perovskites. *Acta Crystallogr., Sect. B: Struct. Sci.* **2005**, *61*, 387–399.
31. Levin, I.; Reaney, I. M. Nano- and Mesoscale Structure of Na1/2Bi1/2TiO3: A TEM Perspective. *Adv. Funct. Mater.* **2012**, *22*, 3445–3452.
32. Sanchez-Santolino, G.; Cabero, M.; Varela, M.; Garcia-Barriocanal, J.; Leon, C.; Pennycook, S. J.; Santamaria, J. Oxygen Octahedral Distortions in LaMO3/SrTiO3 Superlattices. *Microsc. Microanal.* **2014**, *20*, 825–831.
33. Hwang, J.; Zhang, J. Y.; Son, J.; Stemmer, S. Nanoscale Quantification of Octahedral Tilts in Perovskite Films. *Appl. Phys. Lett.* **2012**, *100*, 191909.
34. Yacoby, Y.; Sowwan, M.; Stern, E.; Cross, J. O.; Brewe, D.; Pindak, R.; Pitney, J.; Dufresne, E. M.; Clarke, R. Direct Determination of Epitaxial Interface Structure in Gd2O3 Passivation of GaAs. *Nat. Mater.* **2002**, *1*, 99–101.
35. LeBeau, J. M.; Findlay, S. D.; Allen, L. J.; Stemmer, S. Position Averaged Convergent Beam Electron Diffraction: Theory and Applications. *Ultramicroscopy* **2010**, *110*, 118–125.
36. Borisevich, A. Y.; Ovchinnikov, O. S.; Chang, H. J.; Oxley, M. P.; Yu, P.; Seidel, J.; Eliseev, E. A.; Morozovska, A. N.;

Ramesh, R.; Pennycook, S. J.; et al. Mapping Octahedral Tilts and Polarization across a Domain Wall in BiFeO3 from Z-Contrast Scanning Transmission Electron Microscopy Image Atomic Column Shape Analysis. *ACS Nano* **2010**, *4*, 6071–6079.
37. Kirkland, E. J. *Advanced Computing in Electron Microscopy*; Springer Science & Business Media: Dordrecht, Netherlands, 2010.
38. Woodward, P. M. POTATO – a Program for Generating Perovskite Structures Distorted by Tilting of Rigid Octahedra. *J. Appl. Crystallogr.* **1997**, *30*, 206–207.
39. He, J.; Borisevich, A.; Kalinin, S. V.; Pennycook, S. J.; Pantelides, S. T. Control of Octahedral Tilts and Magnetic Properties of Perovskite Oxide Heterostructures by Substrate Symmetry. *Phys. Rev. Lett.* **2010**, *105*, 227203.
40. Allen, L. J.; D'Alfonso, A. J.; Forbes, B. D.; Findlay, S. D.; LeBeau, J. M.; Stemmer, S. Quantitative Transmission Electron Microscopy at Atomic Resolution. *J. Phys. Conf. Ser.* **2012**, *371*, 012009.
41. LeBeau, J. M.; Findlay, S. D.; Allen, L. J.; Stemmer, S. Quantitative STEM: Experimental Methods and Applications. *J. Phys. Conf. Ser.* **2012**, *371*, 012053.
42. Ishikawa, R.; Mishra, R.; Lupini, A. R.; Findlay, S. D.; Taniguchi, T.; Pantelides, S. T.; Pennycook, S. J. Direct Observation of Dopant Atom Diffusion in a Bulk Semiconductor Crystal Enhanced by a Large Size Mismatch. *Phys. Rev. Lett.* **2014**, *113*, 155501.
43. Sadakane, M.; Endo, K.; Kodato, K.; Ishikawa, S.; Murayama, T.; Ueda, W. Assembly of a Pentagonal Polyoxomolybdate Building Block, [Mo 6 O 21] 6-, into Crystalline MoV Oxides. *Eur. J. Inorg. Chem.* **2013**, *2013*, 1731–1736.
44. Ishikawa, R.; Lupini, A. R.; Findlay, S. D.; Pennycook, S. J. Quantitative Annular Dark Field Electron Microscopy Using Single Electron Signals. *Microsc. Microanal.* **2014**, *20*, 99–110.
45. Lee, S.; Oshima, Y.; Sawada, H.; Hosokawa, F.; Okunishi, E.; Kaneyama, T.; Kondo, Y.; Niitaka, S.; Takagi, H.; Tanishiro, Y.; et al. Counting Lithium Ions in the Diffusion Channel of an LiV2O4 Crystal. *J. Appl. Phys.* **2011**, *109*, 113530.
46. Ishida, T.; Kawasaki, T.; Tanji, T.; Ikuta, T. Quantitative Evaluation of Annular Bright-Field Phase Images in STEM. *Microscopy* **2015**, *64*, 121–128.
47. Ishikawa, R.; Lupini, A. R.; Hinuma, Y.; Pennycook, S. J. Large-Angle Illumination STEM: Toward Three-Dimensional Atom-by-Atom Imaging. *Ultramicroscopy* **2015**, *151*, 122–129.
48. Moon, E. J.; Keavney, D. J.; May, S. J. Strain Effects in Narrow Bandwidth Manganites: The Case of Epitaxial $Eu_{0.7}Sr_{0.3}MnO_3$ Thin Films. *Phys. Rev. Appl.* **2014**, *1*, 054006.